


**Electronic structure and resonant inelastic x-ray scattering in osmates. I. Perovskite NaOsO<sub>3</sub>**V. N. Antonov <sup>1</sup>, D. A. Kukusta,<sup>1,2</sup> and L. V. Bekenov<sup>1</sup><sup>1</sup>*G. V. Kurdyumov Institute for Metal Physics of the National Academy of Sciences of Ukraine, 36 Academician Vernadsky Boulevard, UA-03142 Kyiv, Ukraine*<sup>2</sup>*Max Planck Institute for Solid State Research, Heisenbergstrasse 1, 70569 Stuttgart, Germany*

(Received 22 September 2021; revised 4 February 2022; accepted 30 March 2022; published 21 April 2022)

We have investigated the electronic and magnetic properties of the perovskite NaOsO<sub>3</sub> within density functional theory using the generalized gradient approximation while taking into account strong Coulomb correlations in the framework of the fully relativistic spin-polarized Dirac linear muffin-tin orbital band-structure method. NaOsO<sub>3</sub> is a G-type AFM Mott insulator which is characterized by AFM spins canted away from the *c* axis. This magnetic configuration explains the weak ferromagnetism in NaOsO<sub>3</sub>. Despite the large strength of spin-orbit coupling, it has only a small effect on the electronic and magnetic properties of NaOsO<sub>3</sub>. We have also investigated theoretically the resonant inelastic x-ray scattering (RIXS) spectrum at the Os *L*<sub>3</sub> edge. The experimentally measured RIXS spectrum of NaOsO<sub>3</sub> in addition to the elastic scattering peak at 0 eV possesses a sharp feature below 2 eV corresponding to transitions within the Os *t*<sub>2g</sub> levels, a strong intense peak at around 2.8 eV which is from *t*<sub>2g</sub> → *e*<sub>g</sub> transitions, and a wide structure stretching from 6 eV to 12 eV that corresponds to ligand-to-metal charge transfer excitations, *d-d* transitions to Os *t*<sub>2g</sub> and *e*<sub>g</sub> manifolds from the Os *5d*<sub>0</sub> states derived from the “tails” of oxygen *2p* states.

DOI: [10.1103/PhysRevB.105.155144](https://doi.org/10.1103/PhysRevB.105.155144)**I. INTRODUCTION**

Due to the interplay of strong spin-orbit (SO) interactions and electron correlations, various unconventional quantum phases of matter have been observed in *5d* transition metal oxides, such as topological insulators [1–4], Mott insulators [5–9], Weyl semimetals [10–12], and quantum spin liquids [7,13]. In *5d*<sup>5</sup> (Ir<sup>4+</sup>) iridium oxides, iridates, such as Sr<sub>2</sub>IrO<sub>4</sub> or the honeycomb lattice family A<sub>2</sub>IrO<sub>3</sub> (*A* = Na, Li), a strong SO coupling and a moderate Hubbard *U* open a small band gap called the relativistic Mott gap [5,9,14].

One important family among *5d* transition metal compounds is osmates [15–26]. The role of SO coupling and Hubbard Coulomb interaction in osmates is less clear than in iridates. For example, *5d*<sup>3</sup> (Os<sup>5+</sup>) systems are expected to have an orbital singlet with reduced effective SO coupling [27]. The osmate compounds, such as NaOsO<sub>3</sub> or pyrochlore Cd<sub>2</sub>Os<sub>2</sub>O<sub>7</sub>, nonetheless exhibit a metal-insulator transition (MIT) entwined with a particular magnetic order.

The physical properties of NaOsO<sub>3</sub> are quite intriguing. It possesses unusually high Néel temperature *T*<sub>N</sub> = 410 K, which coincides with the metal-insulator transition, with a magnetic moment of 1.0 μ<sub>B</sub> [18,21,28–30]. Initially, a Slater-like mechanism was proposed to explain this unusual MIT behavior [21]. Later it was argued that the MIT transition is better interpreted by a relativistic magnetic Lifshitz mechanism where MIT is driven by magnetic fluctuations and SO-renormalized electron correlations [23,31–33].

Although the electronic structure and magnetic properties of NaOsO<sub>3</sub> are well investigated [18,20–26], there are a number of questions with regard to the nature of the MIT in

NaOsO<sub>3</sub>. For example, it is still not clear whether the spin or electronic excitations remain coherent through the MIT. Vale *et al.* [31,32] by analyzing the temperature dependence of resonant inelastic x-ray scattering (RIXS) spectra below 1.0 eV established that there is a continuous transition from itinerant to localized behavior through the MIT in NaOsO<sub>3</sub> due to a significant renormalization of the magnetic quasi-particle spectral weight over large ranges of momentum and energy. Shi *et al.* [18] discovered a spontaneous magnetization of 0.005 μ<sub>B</sub>/Os at 5 K through the transition to the G-type antiferromagnetic (AFM) configuration which makes NaOsO<sub>3</sub> weakly ferromagnetic (FM). This experimental fact has no theoretical explanation.

Recently Liu *et al.* [26] provided comparative first-principles calculations of NaOsO<sub>3</sub> and LiOsO<sub>3</sub> using the Vienna *Ab initio* Simulation Package [34,35] with taking into account the SO coupling and Coulomb correlations. They investigated structural, electronic, magnetic, and dynamical properties of the two chemically similar osmates. The origin of the different structural (*R3c* vs *Pnma*) properties was explained by using a symmetry-adapted soft-mode analysis. They also clarify that the distinct electronic (metallic vs insulating) properties originate mainly from a cooperative steric and magnetic effect. A pressure-induced structural phase transition from *R3c* to *Pnma* for LiOsO<sub>3</sub> was predicted, whereas for NaOsO<sub>3</sub> the *Pnma* phase was found to be stabilized over the *R3c* phase by increasing pressure.

Springer *et al.* [36] also provide the comparative investigation of spectroscopic properties of the NaOsO<sub>3</sub> and LiOsO<sub>3</sub> paramagnetic phases using a first-principles many-body density functional theory + dynamical mean field theory

(DFT+DMFT) approach. The authors attribute the different spectroscopic properties of the two osmates to their slightly different proximity to a Hund-Mott insulating phase.

In this work we focus our attention on the RIXS properties of osmates. RIXS is a fast developing experimental technique in which one scatters x-ray photons inelastically off matter [37]. Compared to other scattering techniques, RIXS has a number of unique features: It covers a large scattering phase space, is polarization dependent, element and orbital specific, bulk sensitive, and requires only small sample volumes. There has been great progress in the RIXS experiments over the past decades; however, the number of theoretical calculations of RIXS spectra is extremely limited. This fact can be explained by certain difficulty of the calculation of RIXS spectra.

Recently RIXS measurements have been successfully performed at the Os  $L_3$  edge for such osmates as the perovskite  $\text{NaOsO}_3$  [30–32], pyrochlore  $\text{Cd}_2\text{Os}_2\text{O}_7$  [27,38],  $\text{Ca}_3\text{LiOsO}_6$ , and  $\text{Ba}_2\text{YOsO}_6$  [39]. There are some features in common for all the osmates investigated up to now, although these compounds have quite different structural, magnetic, and electronic properties. In addition to the elastic scattering peak at 0 eV their experimentally measured RIXS spectra possess several sharp features: a low-energy peak below 2 eV, which is widely believed to correspond to transitions within the Os  $t_{2g}$  levels, a peak at higher energy from  $t_{2g} \rightarrow e_g$  transitions, and a wide structure stretching above 5 eV and corresponding to ligand-to-metal charge transfer excitations. The comparison between RIXS experiments and theory can provide insight into the nature of  $5d$  electrons and offer some evaluation of the accuracy of the theoretical approach to treat  $5d$  electrons. In some cases sophisticated many-body approaches are needed if satisfactory quantitative agreement is to be achieved.

With the above as background, we have performed calculations to evaluate the RIXS spectra of some osmates. We have divided the work in two papers. Paper I focuses on the description of the used methods and the results for  $\text{NaOsO}_3$ . Paper II [40] is devoted to the electronic structure and RIXS spectra of  $\text{Cd}_2\text{Os}_2\text{O}_7$ . The energy band structure of the osmates is calculated within the *ab initio* approach using the fully relativistic spin-polarized Dirac linear muffin-tin orbital band-structure method. We use both the generalized gradient approximation (GGA) and GGA+ $U$  approaches to investigate the sensitivity of the RIXS results to different treatment of the correlated electrons.

This paper I is organized as follows. The crystal structure of  $\text{NaOsO}_3$  and computational details are presented in Sec. II. Section III presents the electronic and magnetic structures of  $\text{NaOsO}_3$ . In Sec. IV the theoretical investigation of the RIXS spectrum of  $\text{NaOsO}_3$  at the Os  $L_3$  edge is presented, and the theoretical results are compared with experimental measurements. Finally, the results are summarized in Sec. V.

## II. COMPUTATIONAL DETAILS

### A. Resonant inelastic x-ray scattering

Resonant inelastic x-ray scattering refers to the process where the material first absorbs a photon. The system then is excited to a short-lived intermediate state, from which it relaxes radiatively. In an experiment, one studies the x rays

emitted in this decay process. The RIXS intensity can in general be presented in terms of a scattering amplitude as [37]

$$I(\omega, \kappa, \kappa', \epsilon, \epsilon') = \sum_f |T_{fg}(\kappa, \kappa', \epsilon, \epsilon', \omega_\kappa)|^2 \times \delta(E_f + \hbar\omega_{\kappa'} - E_g - \hbar\omega_\kappa), \quad (1)$$

where the delta function enforces energy conservation and the amplitude  $T_{fg}(\kappa, \kappa', \epsilon, \epsilon', \omega_\kappa)$  reflects which excitations are probed and how, for instance, the spectral weights of final state excitations depend on the polarization vectors  $\epsilon$  and  $\epsilon'$  of the incoming and outgoing x rays, respectively.

In the direct RIXS process [37] the incoming photon with energy  $\hbar\omega_\kappa$ , momentum  $\hbar\kappa$ , and polarization  $\epsilon$  excites the solid from the ground to the intermediate state. Finally the outgoing photon with energy  $\hbar\omega_{\kappa'}$ , momentum  $\hbar\kappa'$ , and polarization  $\epsilon'$  is emitted, and an excitation with energy  $\hbar\omega = \hbar\omega_\kappa - \hbar\omega_{\kappa'}$  and momentum  $\hbar\mathbf{q} = \hbar\kappa - \hbar\kappa'$  is created. As a result the solid stays in the excited state.

The theory of x-ray scattering is based on the second-order golden rule for the transition probability per unit time [41],

$$w = \frac{2\pi}{\hbar} \sum_f \left| \langle f | \hat{H}_{\text{int}} | g \rangle + \sum_I \frac{\langle f | \hat{H}_{\text{int}} | I \rangle \langle I | \hat{H}_{\text{int}} | g \rangle}{E_g - E_I} \right|^2 \times \delta(E_f - E_g); \quad (2)$$

$\hat{H}_{\text{int}}$  is the time-independent part of the photon-electron interaction operator that couples resonant “no-photon”  $|I_0\rangle$  and nonresonant “two-photon”  $|I_{\kappa\epsilon, \kappa'\epsilon'}\rangle$  intermediate states. The formalism to reduce this general expression to a single-electron-like form has been published in Ref. [42]. Therefore we present here only the equations that are key to the present implementation. In the dipolar approximation the operator  $\hat{H}_{\text{int}}$

$$\hat{H}_{\text{int}}(\hat{\mathbf{r}}) = \sum_{\mathbf{R}} \sum_{\kappa\epsilon} \hat{\alpha}\epsilon^\dagger e^{-i\kappa\mathbf{R}} \hat{a}_{\kappa\epsilon}^\dagger + \hat{\alpha}\epsilon e^{i\kappa\mathbf{R}} \hat{a}_{\kappa\epsilon}, \quad (3)$$

where  $\hat{\alpha}$  are Dirac matrices. The operator couples the initial  $|g\rangle$  and final  $|f\rangle$  one-photon states. For them  $\langle f | \hat{H}_{\text{int}} | g \rangle = 0$ .

In the RIXS process in the intermediate state with  $K = (\kappa, \mu)$  the core hole is created, and the sum over  $I_0$  in (2) actually runs over its possible  $\mu$  values. One gets the expression for the RIXS intensity in the dipolar approximation as

$$I = \sum_{n'nk} \left| \sum_{\mu} \frac{\langle \Psi_K | \hat{H}_{\text{int}} | \Psi_{n'k+q} \rangle \langle \Psi_{nk} | \hat{H}_{\text{int}} | \Psi_K \rangle}{\epsilon_\mu + \hbar\omega - E_{nk} + i\Gamma/2} \right|^2 \times \delta(E_{nk} - E_{n'k+q} - \hbar\omega), \quad (4)$$

where  $n'$  and  $n$  denote occupied and empty electronic levels.

The Bloch sum of spin-polarized relativistic Dirac linear muffin-tin orbitals (LMTOs) has the following one-center expansion inside an arbitrary atomic sphere,  $R'$ , with radius  $S_{R'}$ :

$$\chi_{RK}^k(\mathbf{r}) = \sum_{K'} [\Pi_{RK, R'K'}^k \Phi_{R'K'}(\mathbf{r} - \mathbf{R}', E_\nu) + \Omega_{RK, R'K'}^k \dot{\Phi}_{R'K'}(\mathbf{r} - \mathbf{R}', E_\nu)] \quad \text{for} \\ |\mathbf{r} - \mathbf{R}'| \leq S_{R'}; \quad (5)$$

matrices  $\Pi^{\mathbf{k}}$  and  $\Omega^{\mathbf{k}}$  are given in terms of the canonical structure constants [43].  $\Phi_{RK}(\mathbf{r}, E)$  is the solution of the Dirac equation with a spherically symmetric potential,

$$\Phi_K(\mathbf{r}, E) = i^l Z_K(\hat{\mathbf{r}}) \Phi_\kappa(r, E), \quad (6)$$

$\Phi_\kappa(r, E)$  is the matrix of radial solutions,

$$\Phi_\kappa(r, E) = \begin{pmatrix} g_\kappa(r, E) \\ i f_\kappa(r, E) \end{pmatrix}, \quad (7)$$

$Z_K(\hat{\mathbf{r}})$  is the matrix of the spin-angular functions,

$$Z_K(\hat{\mathbf{r}}) = \begin{pmatrix} \chi_\kappa^\mu(\hat{\mathbf{r}}) & 0 \\ 0 & \chi_{-\kappa}^\mu(\hat{\mathbf{r}}) \end{pmatrix}, \quad (8)$$

$$\chi_\kappa^\mu(\hat{\mathbf{r}}) = \sum_{m=\pm 1/2} C_{l, \mu-m, 1/2, m}^{j\mu} Y_{l, \mu-m}(\hat{\mathbf{r}}) \chi(m), \quad (9)$$

$C_{l, \mu-m, 1/2, m}^{j\mu}$  are the Clebsch-Gordan coefficients,  $Y_{lm}(\hat{\mathbf{r}})$  are the spherical harmonics,  $j$  is the eigenvalue of the operator of the total angular momentum  $j = l \pm 1/2$ , and

$$\chi\left(\frac{1}{2}\right) = \begin{pmatrix} 1 \\ 0 \end{pmatrix}, \quad \chi\left(-\frac{1}{2}\right) = \begin{pmatrix} 0 \\ 1 \end{pmatrix}$$

are the Pauli spinors.

Introducing new coefficients

$$A_{RK}^{n\mathbf{k}}(\mathbf{r}) = \sum_{R'K'} \Pi_{RK, R'K'}^{\mathbf{k}} C_{R'K'}^{n\mathbf{k}}, \quad (10)$$

$$B_{RK}^{n\mathbf{k}}(\mathbf{r}) = \sum_{R'K'} \Omega_{RK, R'K'}^{\mathbf{k}} C_{R'K'}^{n\mathbf{k}}, \quad (11)$$

we can express the valence electron wave function in a crystal as

$$\Psi_{n\mathbf{k}}(\mathbf{r}) = \sum_K [A_{RK}^{n\mathbf{k}} \Phi_{RK}(\mathbf{r} - \mathbf{R}, E_v) + B_{RK}^{n\mathbf{k}} \dot{\Phi}_{RK}(\mathbf{r} - \mathbf{R}, E_v)] \quad \text{for } |\mathbf{r} - \mathbf{R}| \leq S_R; \quad (12)$$

here  $\dot{\Phi} \equiv \partial\Phi/\partial E$ .

The matrix element is an integral over the primitive cell. With relativistic LMTOs as basis functions, we express this integral in the standard way as the integral over the interstitial region, where the relativistic LMTOs are free-space solutions, plus the sum of integrals over the atomic spheres, i.e.,

$$\langle \Psi_{n\mathbf{k}} | \hat{H}_{\text{int}} | \Psi_K \rangle = \langle \Psi_{n\mathbf{k}} | \hat{H}_{\text{int}} | \Psi_K \rangle_I + \sum_{\mathbf{R}} \langle \Psi_{n\mathbf{k}} | \hat{H}_{\text{int}} | \Psi_K \rangle_{\mathbf{R}}. \quad (13)$$

In the case of x-ray absorption and RIXS spectra we have transitions between valent and core states. Core states are well localized in the atomic sphere; therefore the integral over the interstitial region can be omitted. Moreover for core states  $\dot{\Phi} \equiv 0$ . The core wave function is

$$\Psi_K(\mathbf{r}) = \begin{pmatrix} g_\kappa(r) \chi_{\kappa\mu}(\hat{\mathbf{r}}) \\ i f_\kappa(r) \chi_{\bar{\kappa}\mu}(\hat{\mathbf{r}}) \end{pmatrix}. \quad (14)$$

For the integral over the atomic sphere at  $\mathbf{R}$ , we obtain from the one-center expansion (12)

$$\langle \Psi_{n\mathbf{k}} | \hat{\alpha}\epsilon | \Psi_K \rangle_{\mathbf{R}} = \sum_{K'} [A_{RK'}^{*n\mathbf{k}} I_{K'K} + B_{RK'}^{*n\mathbf{k}} \dot{I}_{K'K}]. \quad (15)$$

Here

$$I_{K'K} = \langle \Phi_{K'} | \hat{\alpha}\epsilon | \Psi_K \rangle_{\mathbf{R}},$$

$$\dot{I}_{K'K} = \langle \dot{\Phi}_{K'} | \hat{\alpha}\epsilon | \Psi_K \rangle_{\mathbf{R}}.$$

Using the relations  $\alpha = \tau\sigma = \tau\sigma_r(\frac{\mathbf{r}}{r} + [\hat{K}, \frac{\mathbf{r}}{r}])$  we have [44]

$$I_{K'K} = i \langle K' | \hat{\mathbf{r}} | K \rangle \int_0^S \{ [\kappa' - \kappa - 1] g_{\kappa'}(r) f_\kappa(r) + [\kappa' - \kappa + 1] f_{\kappa'}(r) g_\kappa(r) \} r^2 dr,$$

$$\dot{I}_{K'K} = i \langle K' | \hat{\mathbf{r}} | K \rangle \int_0^S \{ [\kappa' - \kappa - 1] \dot{g}_{\kappa'}(r) f_\kappa(r) + [\kappa' - \kappa + 1] \dot{f}_{\kappa'}(r) g_\kappa(r) \} r^2 dr,$$

with

$$\langle K' | \hat{\mathbf{r}} | K \rangle = i^{l-l'} \langle \chi_{\kappa'}^{l'} | \hat{\mathbf{r}} | \chi_\kappa^l \rangle.$$

The matrix elements in (4) are expressed as the lattice sum

$$\begin{aligned} \langle \Psi_{n\mathbf{k}} | \hat{H}_{\text{int}} | \Psi_K \rangle &= \sum_{\mathbf{R}} e^{i\mathbf{k}\mathbf{R}} \langle \Psi_{n\mathbf{k}} | \hat{\alpha}\epsilon | \Psi_K \rangle_{\mathbf{R}} \\ &= \sum_{\mathbf{R}} e^{i\mathbf{k}\mathbf{R}} \sum_{K'} [A_{RK'}^{*n\mathbf{k}} I_{K'K} + B_{RK'}^{*n\mathbf{k}} \dot{I}_{K'K}], \end{aligned}$$

$$\begin{aligned} \langle \Psi_K | \hat{H}_{\text{int}} | \Psi_{n'\mathbf{k}+\mathbf{q}} \rangle &= \sum_{\mathbf{R}} e^{-i\mathbf{k}'\mathbf{R}} \langle \Psi_K | \hat{\alpha}\epsilon^{*} | \Psi_{n'\mathbf{k}+\mathbf{q}} \rangle_{\mathbf{R}} \\ &= \sum_{\mathbf{R}} e^{-i\mathbf{k}'\mathbf{R}} \sum_{K'} [A_{RK'}^{n'\mathbf{k}+\mathbf{q}} I_{K'K}^* + B_{RK'}^{n'\mathbf{k}+\mathbf{q}} \dot{I}_{K'K}^*]; \end{aligned}$$

their product allows us to write down the Bragg factor explicitly:

$$\langle \Psi_K | \hat{H}_{\text{int}} | \Psi_{n'\mathbf{k}+\mathbf{q}} \rangle \langle \Psi_{n\mathbf{k}} | \hat{H}_{\text{int}} | \Psi_K \rangle = \sum_{\mathbf{R}} f_{\mathbf{R}}^{\mathbf{k}} e^{i\mathbf{q}\mathbf{R}},$$

where

$$\begin{aligned} f_{\mathbf{R}}^{\mathbf{k}} &= \sum_{K''K'} [A_{RK''}^{*n\mathbf{k}} I_{K''K} + B_{RK''}^{*n\mathbf{k}} \dot{I}_{K''K}] \\ &\quad \times [A_{RK'}^{n'\mathbf{k}+\mathbf{q}} I_{K'K}^* + B_{RK'}^{n'\mathbf{k}+\mathbf{q}} \dot{I}_{K'K}^*] \\ &= \sum_{K''K'} [A_{RK''}^{*n\mathbf{k}} A_{RK'}^{n'\mathbf{k}+\mathbf{q}} I_{K''K}^* I_{K'K} \\ &\quad + A_{RK''}^{*n\mathbf{k}} B_{RK'}^{n'\mathbf{k}+\mathbf{q}} I_{K''K}^* \dot{I}_{K'K} \\ &\quad + A_{RK''}^{n'\mathbf{k}+\mathbf{q}} B_{RK'}^{*n\mathbf{k}} I_{K''K} \dot{I}_{K'K} \\ &\quad + B_{RK''}^{n'\mathbf{k}+\mathbf{q}} B_{RK'}^{*n\mathbf{k}} \dot{I}_{K''K} \dot{I}_{K'K}]. \end{aligned}$$

Finally one gets for the RIXS intensity (4)

$$I = \sum_{n'\mathbf{k}} \left| \sum_{\mathbf{R}} e^{i\mathbf{q}\mathbf{R}} \sum_{\mu} \frac{f_{\mathbf{R}}^{\mathbf{k}}}{\varepsilon_{\mu} + \hbar\omega - E_{n\mathbf{k}} + i\Gamma/2} \right|^2 \times \delta(E_{n\mathbf{k}} - E_{n'\mathbf{k}+\mathbf{q}} - \hbar\omega).$$

More detailed expressions of the matrix elements in the electric dipole approximation may be found in Refs. [41,44–46]. The matrix elements due to the magnetic dipole and electric quadrupole corrections are presented in Ref. [41].

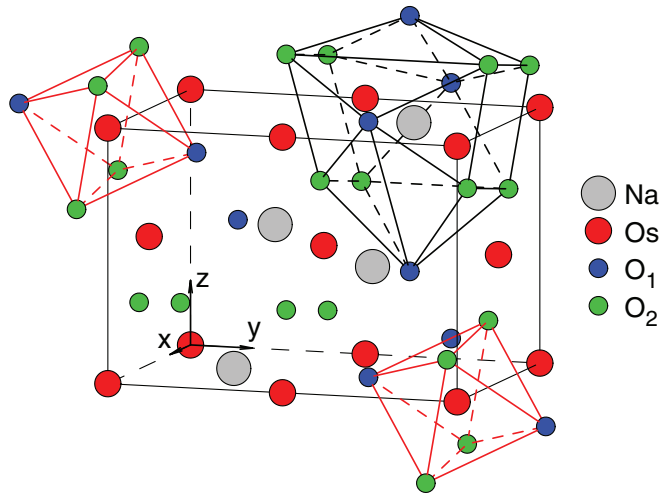


FIG. 1. The crystal structure of  $\text{NaOsO}_3$  (the space group is  $Pnma$ , No. 62) [18]. Red spheres represent osmium atoms, blue and green spheres show oxygen atoms, gray spheres represent Na atoms.

### B. Crystal structure

The composition of  $\text{NaOsO}_3$  in the orthorhombic structure was obtained in 2008 [18]. Figure 1 presents  $\text{NaOsO}_3$  in the orthorhombic perovskite structure with space group  $Pnma$ , and with Na atoms at the  $4c$  position (0.0328, 0.25,  $-0.0065$ ), Os at the  $4b$  position (0, 0, 0.5),  $\text{O}_1$  at the  $4c$  (0.4834, 0.25, 0.0808), and  $\text{O}_2$  at the  $8d$  (0.2881, 0.0394, 0.7112) positions. In each unit cell there are four formula units (f.u.). The unit-cell parameters in  $\text{NaOsO}_3$  are equal to  $a = 5.38420 \text{ \AA}$ ,  $b = 7.58038 \text{ \AA}$ , and  $c = 5.32817 \text{ \AA}$  [18]. The Os atoms have two  $\text{O}_1$  atoms as nearest neighbors (at 1.9454  $\text{\AA}$  distance) and four  $\text{O}_2$  atoms as nearest neighbors (at 1.9387  $\text{\AA}$  distance), while for Na there are four  $\text{O}_1$  atoms (at 2.2837  $\text{\AA}$ , 2.4703  $\text{\AA}$ , 2.9944  $\text{\AA}$ , and 3.0715  $\text{\AA}$  distances) and four pairs of  $\text{O}_2$  atoms (at 2.3397  $\text{\AA}$ , 2.588  $\text{\AA}$ , 2.6623  $\text{\AA}$ , and 3.2052  $\text{\AA}$  distances).

The O-Os-O bond angles are  $90.7^\circ$ ,  $89.3^\circ$ , or  $89.1^\circ$ , indicating nearly ideal  $\text{OsO}_6$  octahedra. The  $\text{OsO}_6$  octahedra show both tilts and rotations, which vary between different octahedra in the unit cell. The O-Os-O axis is tilted by  $11^\circ$  relative to the  $b$  axis and is rotated by  $9^\circ$  around the  $a$  (or  $c$ ) axis. The magnitudes of these angles are the same for different octahedra, but their signs change between the four octahedra in the  $ac$  plane. The other four octahedra in the unit cell are displaced along the  $z$  direction and have the same pattern of rotation, but their tilts are opposite.

Sereika *et al.* [33] using combined electrical resistance, Raman, and synchrotron x-ray diffraction experiments show that the insulating ground state in  $\text{NaOsO}_3$  endures under high pressure up to at least 35 GPa. The structural change from a centrosymmetric  $Pnma$  to a noncentrosymmetric (polar)  $Pna2_1$  phase takes place at 18 GPa. The high-pressure phase has more distorted octahedra than the phase at the ambient pressure. The density functional theory calculations show that upon pressure the indirect gap is closed at around 20 GPa, while the direct gap survives even up to very high pressure, indicating the insulator to bad metal (BM) transition upon pressure [33].

### C. Calculation details

The details of the computational method are described in our previous papers [47–50] and here we only mention several aspects. The band structure calculations were performed using the fully relativistic linear muffin-tin orbital method [43,46]. This implementation of the LMTO method uses four-component basis functions constructed by solving the Dirac equation inside an atomic sphere [51]. The exchange-correlation functional of the generalized gradient approximation (GGA) type was used in the version of Perdew, Burke, and Ernzerhof [52]. The Brillouin zone integration was performed using the improved tetrahedron method [53]. The basis consisted of Os  $s$ ,  $p$ ,  $d$ , and  $f$ ; and Na and O  $s$ ,  $p$ , and  $d$  LMTOs.

To take into account the electron-electron correlation effects we used in this work the “relativistic” generalization of the rotationally invariant version of the LSDA+ $U$  method [54], which takes into account that in the presence of spin-orbit coupling the occupation matrix of localized electrons becomes nondiagonal in spin indexes. We use in our calculations the value of the exchange Hund coupling  $J_H = 0.7 \text{ eV}$  obtained from constrained LSDA calculations [55,56]. Hubbard  $U$  was considered as an external parameter and varied from 0.7 eV to 4.7 eV. Thus, the parameter  $U_{\text{eff}} = U - J_H$ , which roughly determines the splitting between the lower and upper Hubbard bands, varied between 0 eV and 4.0 eV. We adjusted the value of  $U$  to achieve the best agreement with the experiment.

In the RIXS process an electron is promoted from a core level to an intermediate state, leaving a core hole. As a result, the electronic structure at this state differs from that of the ground state. In order to reproduce the experimental spectrum the self-consistent calculations should be carried out including a core hole. In this study the core-hole effect was fully taken into account in the self-consistent iterations by removing an electron at the core orbital using the supercell approximation. The interaction and the screening of the electron-hole pair are fully accounted for by the self-consistent iterations of the final state Kohn-Sham equations. Such an approach considers the symmetry breaking of the system in a natural way, and self-consistently describes the charge redistribution induced by the core hole. A similar approximation has been used by several authors [57–63] for the interpretation of the x-ray absorption. However, the effect of the electron-hole interaction in the intermediate state on the RIXS spectra has been investigated to a much lesser extent in the literature. One should mention that the effect of the electron-hole interaction can be different for different edges and systems with different localization of the electronic states. We note also that the size of the supercell is important, and it should be large enough to inhibit the interaction between excited atoms in neighboring supercells. In our calculations we used a  $1 \times 1 \times 2$  supercell. At one of eight Os atoms we created a hole at the  $2p_{3/2}$  level for the self-consistent GGA+ $U$  calculations of the  $L_3$  spectra.

## III. ELECTRONIC AND MAGNETIC STRUCTURES

In order to gain insight about the ground state magnetic configurations of  $\text{NaOsO}_3$  we compared the calculated



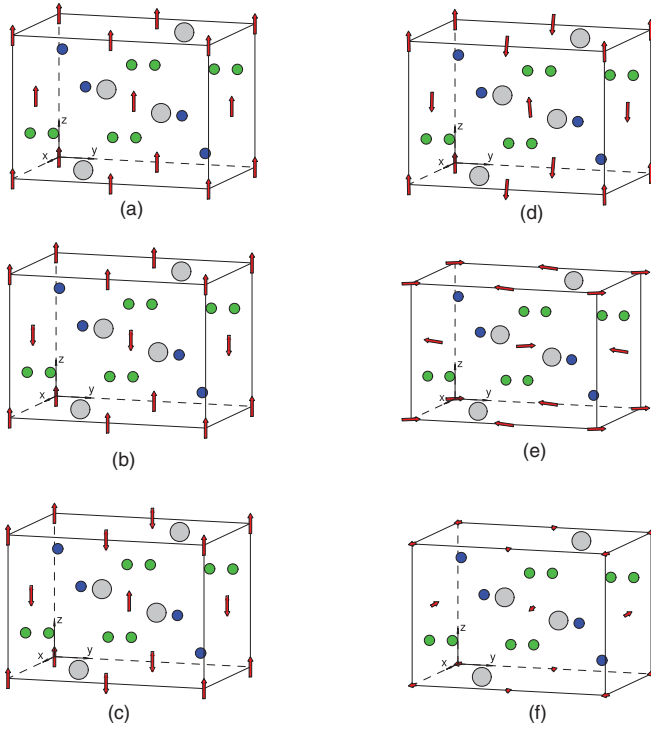


FIG. 2. Magnetic configurations in  $\text{NaOsO}_3$ : FM (a), A-AFM<sub>001</sub> (b), G-AFM<sub>001</sub> (c), G-NCM<sub>001</sub> (d), and G-NCM<sub>100</sub> (e). Red arrows show osmium spin orientations, blue and green spheres show oxygen atoms, gray spheres represent Na atoms.

total energies for different spin ordering in  $\text{NaOsO}_3$ , namely, nonmagnetic, FM, AFM, and possible noncollinear magnetic (NCM). For AFM phases we consider two types of ordering along the  $c$  axis: the A-type AFM state (A-AFM) with layers of Os ions coupled ferromagnetically in a given set of (001) planes but with alternate planes having opposite spin orientation, and the G-type AFM state (G-AFM) with Os ions coupled antiferromagnetically with all of their nearest neighbors (see Fig. 2). We also consider the same AFM ordering along the  $a$  and  $b$  axis. We found that GGA without the SO coupling gives a magnetic solution only for G-AFM ordering. The SO coupling suppresses magnetization even for the G-AFM state. Besides, both the approximations produce a metallic ground state in  $\text{NaOsO}_3$  (the upper panel of Fig. 3) in contradiction with resistivity and optical measurements [28], which claim that  $\text{NaOsO}_3$  is an insulator. To produce the insulating magnetic ground state one has to take into account Coulomb electron correlations. The GGA+SO+ $U$  produces a magnetic insulating solution in  $\text{NaOsO}_3$ . The G-AFM configuration possesses the lowest total energy in comparison with the FM or all the other AFM configurations under consideration (Table I). The energy gap opens with Hubbard  $U = 1.7$  eV ( $U_{\text{eff}} = 1.0$  eV) in agreement with Shi *et al.* [18] calculations.

We should mention that the G-AFM ground state is still in contradiction with the isothermal magnetization measurements by Shi *et al.* [18] which display the spontaneous magnetization of  $0.005 \mu_B/\text{Os}$  at 5 K, because any AFM ordering produces zero net magnetization in the system. Applying the noncollinear formalism [64,65] to  $\text{NaOsO}_3$  we found a G-NCM state with the total energy lower by several

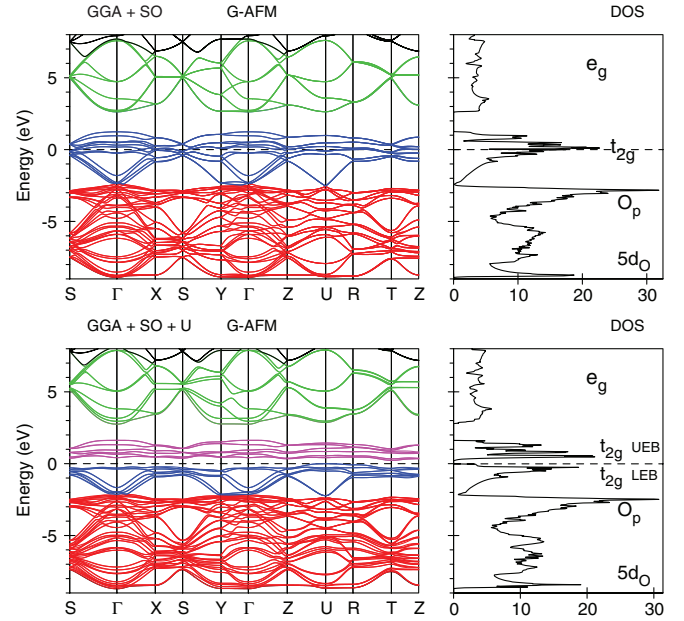


FIG. 3. The energy band structure and total DOSs of G-AFM  $\text{NaOsO}_3$  calculated in GGA+SO (the upper panel) and GGA+SO+ $U$  ( $U_{\text{eff}} = 1.5$  eV) for the G-NCM structure (the lower panel).

meV in comparison with the G-AFM configuration (Table I). This G-NCM state is characterized by AFM spins canted away from the  $c$  axis with the polar angle equal to  $\theta = 5.6^\circ$ . It produces a small projection of the Os spin magnetic moment on the  $ab$  plane of around  $0.097 \mu_B$ . Although this value is larger than the experimental magnetization, it can explain the weak ferromagnetism in  $\text{NaOsO}_3$ . It is important to note that the energy gap in  $\text{NaOsO}_3$  with the G-NCM configuration opens for a smaller value of Hubbard  $U = 0.7$  eV in comparison with the G-AFM ordering.

Figure 4 presents the Os  $5d$  and oxygen  $2p$  partial DOSs of the G-NCM structure calculated in the GGA+SO+ $U$  approximation with  $U_{\text{eff}} = 1.5$  eV. Each  $\text{Os}^{5+}$  ion in  $\text{NaOsO}_3$  surrounded by six  $\text{O}^{2-}$  ions has three valent  $5d$  electrons. The octahedral crystal field splits the Os  $t_{2g}$  and  $e_g$  manifolds, so that three electrons occupy the  $t_{2g}$  low energy band (LEB) manifold in the energy interval from  $-2.1$  eV to 0 eV. The

TABLE I. The total energy  $E_{\text{total}}$  per formula unit (in eV), defined relative to the G-NCM<sub>001</sub> configuration, as well as the theoretical direct ( $\Delta E_{\text{dir}}$ ) and indirect ( $\Delta E_{\text{indir}}$ ) energy gaps (in eV) for several magnetic configurations calculated using the GGA+ $U$ +SO method with  $U_{\text{eff}} = 1.5$  eV.

Magnetic configuration	$E_{\text{total}}$ (eV)	$\Delta E_{\text{dir}}$	$\Delta E_{\text{indir}}$
NM	0.520	0	0
FM <sub>001</sub>	0.222	0.326	0.254
A-AFM <sub>001</sub>	0.175	0.466	0.257
G-AFM <sub>001</sub>	0.015	0.440	0.214
G-NCM <sub>010</sub>	0.006	0.580	0.451
G-NCM <sub>100</sub>	0.005	0.630	0.437
G-NCM <sub>001</sub>	0	0.681	0.552

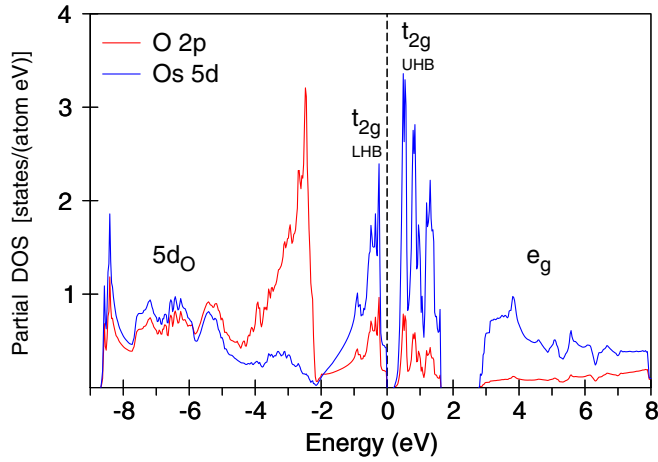


FIG. 4. The Os 5d and oxygen 2p partial DOSs for NaOsO<sub>3</sub> calculated in the GGA+SO+ $U$  ( $U_{\text{eff}} = 1.5$  eV) approximation for the G-NCM structure.

$t_{2g}$  upper energy band (UEB) occupies the energy range from 0.07 eV to 1.6 eV. The  $e_g$  states spread from 2.8 eV to 8 eV. The oxygen 2p states are located from  $-8.7$  eV to  $-2.1$  eV. The occupation number of the  $t_{2g}$  LEB at  $-2.1$  eV to 0 eV is  $n = 2.81$ , which corresponds to a  $5d^3$  configuration of the Os ion. The total 5d charge in the Os atomic sphere is, however, equal to 5.26. The excessive 5d charge of 2.45 electrons comes mainly from the “tails” of oxygen 2p electrons distributed over the energy range from  $-8.7$  to  $-2.1$  eV. These  $5d_O$  states play an essential role in the RIXS spectrum at the Os  $L_3$  edge (see Sec. IV).

Table II presents the theoretically calculated Os spin  $M_s$ , orbital  $M_l$ , and total  $M_{\text{tot}}$  magnetic moments in NaOsO<sub>3</sub> as well as the theoretical direct and indirect energy gaps. Our GGA+SO+ $U$  calculations produce the insulator solution in NaOsO<sub>3</sub> in agreement with the experimental data but slightly overestimate the direct gap in comparison with the optical measurements [28]. The low-energy high-resolution RIXS for NaOsO<sub>3</sub> [30] shows an indirect spin gap of 0.058 eV, which is

TABLE II. The theoretically calculated Os spin  $M_s$ , orbital  $M_l$ , and total  $M_{\text{tot}}$  magnetic moments (in  $\mu_B$ ) in NaOsO<sub>3</sub> as well as the theoretical direct ( $\Delta E_{\text{dir}}$ ) and indirect ( $\Delta E_{\text{indir}}$ ) energy gaps (in eV) calculated for the noncollinear G-NCM ordering. The experimental value of the total magnetic moment is equal to  $1.0 \pm 0.1 \mu_B$  [21]; the experimental direct optical gap is equal to 0.102 eV [28], indirect gap is equal to 0.058 eV [30].

$U_{\text{eff}}$ (eV)	Magnetic moments ( $\mu_B$ )			Energy gap (eV)	
	$M_s$	$M_l$	$M_{\text{tot}}$	$\Delta E_{\text{dir}}$	$\Delta E_{\text{indir}}$
0.0	1.223	-0.098	1.125	0.267	0.067
0.1	1.263	-0.100	1.163	0.305	0.101
0.2	1.350	-0.104	1.246	0.402	0.185
0.5	1.398	-0.106	1.292	0.451	0.244
1.0	1.527	-0.112	1.415	0.626	0.427
1.5	1.627	-0.117	1.510	0.681	0.552
2.0	1.707	-0.121	1.586	0.941	0.792

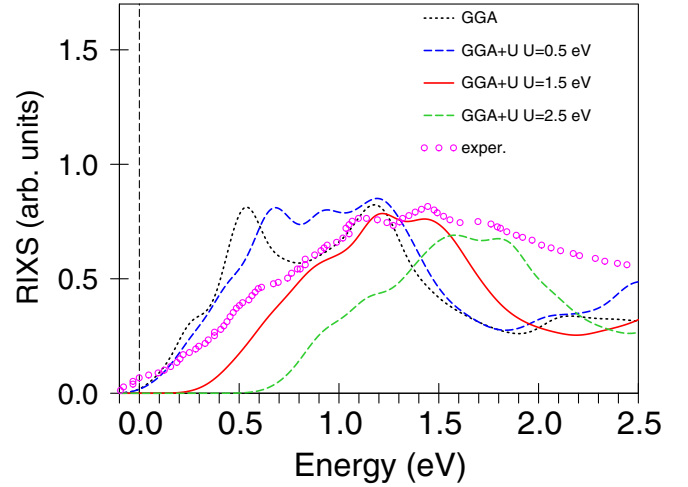


FIG. 5. The experimental RIXS spectrum measured by Calder *et al.* [30] (open magenta circles) at the Os  $L_3$  edge of NaOsO<sub>3</sub> for the  $t_{2g} \rightarrow t_{2g}$  transitions calculated in the GGA and GGA+SO+ $U$  ( $U_{\text{eff}} = 0.5, 1.5,$  and  $2.5$  eV) approximations with taking into account the core-hole effect.

in good agreement with our GGA+SO+ $U$  calculations (with  $U_{\text{eff}} = 0$  eV). The magnetic moments as well as the energy gaps increase with increasing Hubbard  $U$ .

#### IV. Os $L_3$ RIXS SPECTRA

The experimentally measured RIXS spectrum at the Os  $L_3$  edge consists of the peak centered at zero energy loss, which comprises the elastic line and other low-energy features such as phonons, magnons, etc., and three inelastic excitations centered at 1.27 eV, 3.6 eV, and between 6 eV and 12 eV ( $E_B$ ,  $E_C$ ,  $E_D$ , and  $\alpha$ ,  $\beta$ ,  $\gamma$  peaks according to Refs. [30] and [32], respectively).

The low-energy peak  $\alpha$  corresponds to intra- $t_{2g}$  transitions. This peak is very sensitive to the value of the energy gap in NaOsO<sub>3</sub> and the relative position of the  $t_{2g}$  LEB and UEB bands (Fig. 4). Figure 5 shows the experimental RIXS spectrum measured by Calder *et al.* [30] (open magenta circles) compared with the theoretical spectra calculated for the  $t_{2g} \rightarrow t_{2g}$  transitions with taking into account of the core-hole effect. The core hole significantly reduces the value of the magnetic moment at the excited site and destroys the AFM ordering changing it to ferrimagnetic (FiM). The new magnetic order influences the electronic structure of NaOsO<sub>3</sub>. The best agreement between the theoretically calculated and experimental RIXS spectra was achieved for  $U_{\text{eff}} = 1.5$  eV (the full red line in Fig. 5). Actually, the same Hubbard parameter was found to be typical in some iridates, such as  $\beta$ -Li<sub>2</sub>IrO<sub>3</sub> [14,66] or pyrochlore iridates [50]. The calculations with  $U_{\text{eff}} = 0.5$  eV and  $2.5$  eV shift the RIXS spectrum toward lower and higher energies, respectively. The GGA+SO approach produces the metallic ground state, and the corresponding spectrum (the black dotted line) is in poor agreement with the experimental data.

It is interesting to note that the core-hole effect and Hubbard  $U$  affect the position only of the first two peaks  $\alpha$  and  $\beta$ , which reflect the  $d$ - $d$  transitions. The position of the third peak

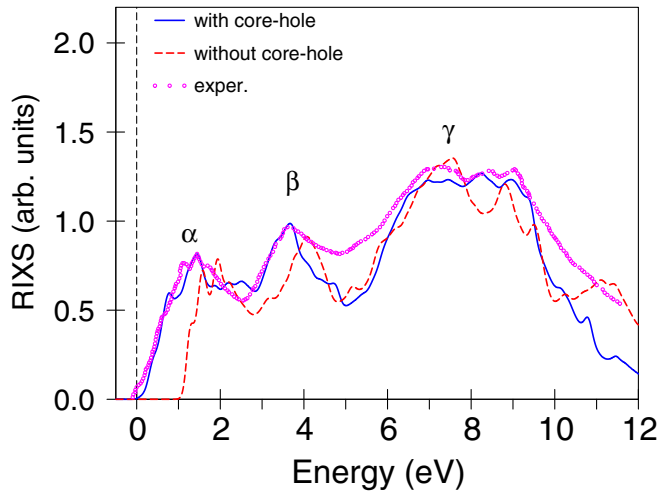


FIG. 6. The experimental RIXS spectrum (open magenta circles) at the Os  $L_3$  edge for NaOsO<sub>3</sub> [30] compared with the theoretical spectra for the G-NCM state with (the full blue line) and without (the dashed red line) taking into account the core-hole effect calculated in the GGA+SO+ $U$  ( $U_{\text{eff}} = 1.5$  eV) approximation.

$\delta$  does not depend on  $U$  and the core-hole effect because this peak reflects the charge-transfer transitions. Still the core-hole effect slightly improves the shape of the  $\delta$  peak (Fig. 6).

Figure 7 presents the experimental RIXS spectrum (open magenta circles) at the Os  $L_3$  edges for NaOsO<sub>3</sub> [30] compared with the theoretical spectrum (the full blue line) as well as the partial contributions from different interband transitions calculated in the GGA+SO+ $U$  ( $U_{\text{eff}} = 1.5$  eV) approximation. We found that the excitation  $\beta$  located at 3.6 eV is due to  $t_{2g} \rightarrow e_g$  transitions, and therefore it gives a direct measure of the crystal field splitting in NaOsO<sub>3</sub>. The third wide structure  $\gamma$  situated from 6 eV to 12 eV appears due to the ligand-to-metal charge transfer excitations,  $d-d$  transitions to Os  $t_{2g}$  and  $e_g$  manifolds from the Os  $5d_O$  states derived from the “tails” of oxygen  $2p$  states.

## V. CONCLUSIONS

The electronic and magnetic structures of the perovskite NaOsO<sub>3</sub> were investigated theoretically using first-principles calculations in the frame of the fully relativistic spin-polarized Dirac LMTO band-structure method in order to understand the importance of Coulomb interaction, spin-orbit coupling, and magnetic order in its temperature-induced and magnetic-related metal-insulator transition.

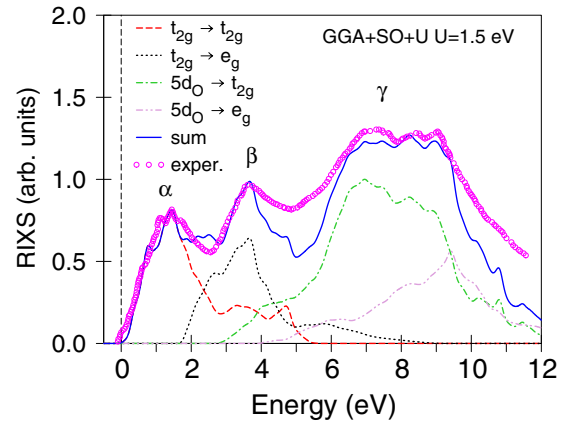


FIG. 7. The experimental RIXS spectrum at the Os  $L_3$  edges for NaOsO<sub>3</sub> measured by Calder *et al.* [30] (open magenta circles) compared with the theoretical spectrum (the full blue line) calculated in the GGA+SO+ $U$  ( $U_{\text{eff}} = 1.5$  eV) approximation and the partial contributions from different interband transitions.

NaOsO<sub>3</sub> is a G-type AFM Mott insulator which is characterized by AFM spins canted away from the  $c$  axis (the G-NCM configuration). This magnetic configuration explains the weak ferromagnetism in NaOsO<sub>3</sub>. Despite the large strength of spin-orbit coupling, it has only a small effect on the electronic and magnetic properties of NaOsO<sub>3</sub>.

The experimentally measured RIXS spectrum at the Os  $L_3$  edge of NaOsO<sub>3</sub> in addition to the elastic scattering peak at 0 eV possesses three inelastic excitations  $\alpha$ ,  $\beta$ , and  $\gamma$  centered at 1.27 eV, 3.6 eV, and between 6 eV and 12 eV, respectively. The low-energy peak  $\alpha$  corresponds to intra- $t_{2g}$  transitions. The excitation  $\beta$  located at 3.6 eV is due to  $t_{2g} \rightarrow e_g$  transitions, and therefore it gives a direct measure of the crystal field splitting in NaOsO<sub>3</sub>. The third wide structure  $\gamma$  situated from 6 eV to 12 eV appears due to the ligand-to-metal charge transfer excitations,  $d-d$  transitions to Os  $t_{2g}$  and  $e_g$  manifolds from the Os  $5d_O$  states derived from the “tails” of oxygen  $2p$  states. Our GGA+SO+ $U$  calculations with  $U_{\text{eff}} = 1.5$  eV for the G-NCM ordering reproduce relatively well the shape of the experimental RIXS spectrum [30].

## ACKNOWLEDGMENTS

D.A.K. gratefully acknowledges the hospitality at the Max Planck Institute for Solid State Research in Stuttgart during his stay there. The studies were supported by the National Academy of Sciences of Ukraine within the budget program KPKBK 6541230 “Support for the development of priority areas of scientific research.”

- [1] X.-L. Qi and S.-C. Zhang, *Phys. Today* **63**(1), 33 (2010).  
 [2] Y. Ando, *J. Phys. Soc. Jpn.* **82**, 102001 (2013).  
 [3] T. O. Wehling, A. Black-Schafferc, and A. Balatsky, *Adv. Phys.* **63**, 1 (2014).  
 [4] A. Bansil, H. Lin, and T. Das, *Rev. Mod. Phys.* **88**, 021004 (2016).

- [5] B. J. Kim, H. Jin, S. J. Moon, J.-Y. Kim, B.-G. Park, C. S. Leem, J. Yu, T. W. Noh, C. Kim, S.-J. Oh *et al.*, *Phys. Rev. Lett.* **101**, 076402 (2008).  
 [6] B. J. Kim, H. Ohsumi, T. Komesu, S. Sakai, T. Morita, H. Takagi, and T. Arima, *Science* **323**, 1329 (2009).

- [7] G. Jackeli and G. Khaliullin, *Phys. Rev. Lett.* **102**, 017205 (2009).
- [8] H. Watanabe, T. Shirakawa, and S. Yunoki, *Phys. Rev. Lett.* **105**, 216410 (2010).
- [9] C. Martins, M. Aichhorn, L. Vaugier, and S. Biermann, *Phys. Rev. Lett.* **107**, 266404 (2011).
- [10] W. Witczak-Krempa and Y. B. Kim, *Phys. Rev. B* **85**, 045124 (2012).
- [11] A. Go, W. Witczak-Krempa, G. S. Jeon, K. Park, and Y. B. Kim, *Phys. Rev. Lett.* **109**, 066401 (2012).
- [12] A. B. Sushkov, J. B. Hofmann, G. S. Jenkins, J. Ishikawa, S. Nakatsuji, S. Das Sarma, and H. D. Drew, *Phys. Rev. B* **92**, 241108(R) (2015).
- [13] I. Kimchi, J. G. Analytis, and A. Vishwanath, *Phys. Rev. B* **90**, 205126 (2014).
- [14] V. N. Antonov, S. Uba, and L. Uba, *Phys. Rev. B* **98**, 245113 (2018).
- [15] D. Mandrus, J. R. Thompson, R. Gaal, L. Forro, J. C. Bryan, B. C. Chakoumakos, L. M. Woods, B. C. Sales, R. S. Fishman, and V. Keppens, *Phys. Rev. B* **63**, 195104 (2001).
- [16] K.-W. Lee and W. E. Pickett, *Europhys. Lett.* **80**, 37008 (2007).
- [17] A. Koda, R. Kadono, K. Ohishi, S. R. Saha, W. Higemoto, S. Yonezawa, Y. Muraoka, and Z. Hiroi, *J. Phys. Soc. Jpn.* **76**, 063703 (2007).
- [18] Y. G. Shi, Y. F. Guo, S. Yu, M. Arai, A. A. Belik, A. Sato, K. Yamaura, E. Takayama-Muromachi, H. F. Tian, H. X. Yang *et al.*, *Phys. Rev. B* **80**, 161104(R) (2009).
- [19] Y. H. Matsuda, J. L. Her, S. Michimura, T. Inami, M. Suzuki, N. Kawamura, M. Mizumaki, K. Kindo, J. Yamauara, and Z. Hiroi, *Phys. Rev. B* **84**, 174431 (2011).
- [20] Y. Du, X. Wan, L. Sheng, J. Dong, and S. Y. Savrasov, *Phys. Rev. B* **85**, 174424 (2012).
- [21] S. Calder, V. O. Garlea, D. F. McMorrow, M. D. Lumsden, M. B. Stone, J. C. Lang, J.-W. Kim, J. A. Schlueter, Y. G. Shi, K. Yamaura *et al.*, *Phys. Rev. Lett.* **108**, 257209 (2012).
- [22] M.-C. Jung, Y.-J. Song, K.-W. Lee, and W. E. Pickett, *Phys. Rev. B* **87**, 115119 (2013).
- [23] B. Kim, P. Liu, Z. Ergonenc, A. Toschi, S. Khmelevskiy, and C. Franchini, *Phys. Rev. B* **94**, 241113(R) (2016).
- [24] N. Gurung, N. Leo, S. P. Collins, G. Nisbet, G. Smolentsev, M. García-Fernández, K. Yamaura, L. J. Heyderman, U. Staub, Y. Joly *et al.*, *Phys. Rev. B* **98**, 115116 (2018).
- [25] S. Dobrovits, B. Kim, M. Retliccioli, A. Toschi, S. Khmelevskiy, and C. Franchini, *J. Phys.: Condens. Matter* **31**, 244002 (2019).
- [26] P. Liu, J. He, B. Kim, S. Khmelevskiy, A. Toschi, G. Kresse, and C. Franchini, *Phys. Rev. Materials* **4**, 045001 (2020).
- [27] S. Calder, J. Vale, N. Bogdanov, X. Liu, C. Donnerer, M. Upton, D. Casa, A. Said, M. Lumsden, Z. Zhao *et al.*, *Nat. Commun.* **7**, 11651 (2016).
- [28] I. L. Vecchio, A. Perucchi, P. D. Pietro, O. Limaj, U. Schade, Y. Sun, M. Arai, K. Yamaura, and S. Lupi, *Sci. Rep.* **3**, 2990 (2013).
- [29] S. Middey, S. Debnath, P. Mahadevan, and D. D. Sarma, *Phys. Rev. B* **89**, 134416 (2014).
- [30] S. Calder, J. G. Vale, N. Bogdanov, C. Donnerer, D. Pincini, M. M. Sala, X. Liu, M. H. Upton, D. Casa, Y. G. Shi *et al.*, *Phys. Rev. B* **95**, 020413(R) (2017).
- [31] J. G. Vale, S. Calder, C. Donnerer, D. Pincini, Y. G. Shi, Y. Tsujimoto, K. Yamaura, M. M. Sala, J. van den Brink, A. D. Christianson *et al.*, *Phys. Rev. Lett.* **120**, 227203 (2018).
- [32] J. G. Vale, S. Calder, C. Donnerer, D. Pincini, Y. G. Shi, Y. Tsujimoto, K. Yamaura, M. M. Sala, J. van den Brink, A. D. Christianson *et al.*, *Phys. Rev. B* **97**, 184429 (2018).
- [33] R. Sereika, P. Liu, B. Kim, S. Kim, J. Zhang, B. Chen, K. Yamaura, C. Park, C. Franchini, Y. Ding, and H. Mao, *npj Quantum Mater.* **5**, 66 (2020).
- [34] G. Kresse and J. Hafner, *Phys. Rev. B* **47**, 558 (1993).
- [35] G. Kresse and J. Furthmüller, *Phys. Rev. B* **54**, 11169 (1996).
- [36] D. Springer, B. Kim, P. Liu, S. Khmelevskiy, S. Adler, M. Capone, G. Sangiovanni, C. Franchini, and A. Toschi, *Phys. Rev. Lett.* **125**, 166402 (2020).
- [37] L. J. P. Ament, M. van Veenendaal, T. P. Devereaux, J. P. Hill, and J. van den Brink, *Rev. Mod. Phys.* **83**, 705 (2011).
- [38] J. G. Vale, S. Calder, N. A. Bogdanov, C. Donnerer, M. M. Sala, N. R. Davies, D. Mandrus, J. van den Brink, A. D. Christianson, and D. F. McMorrow, *Phys. Rev. B* **101**, 014441 (2020).
- [39] A. E. Taylor, S. Calder, R. Morrow, H. L. Feng, M. H. Upton, M. D. Lumsden, K. Yamaura, P. M. Woodward, and A. D. Christianson, *Phys. Rev. Lett.* **118**, 207202 (2017).
- [40] V. N. Antonov, D. A. Kukusta, and L. V. Bekenov, *Phys. Rev. B* **105**, 155145 (2022).
- [41] E. Arola, M. Horne, P. Strange, H. Winter, Z. Szotek, and W. M. Temmerman, *Phys. Rev. B* **70**, 235127 (2004).
- [42] E. Arola, P. Strange, and B. L. Gyorffy, *Phys. Rev. B* **55**, 472 (1997).
- [43] O. K. Andersen, *Phys. Rev. B* **12**, 3060 (1975).
- [44] V. N. Antonov, A. I. Bagljuk, A. Y. Perlov, V. V. Nemoshkalenko, V. N. Antonov, O. K. Andersen, and O. Jepsen, *Low Temp. Phys.* **19**, 494 (1993).
- [45] G. Y. Guo, H. Ebert, W. M. Temmerman, and P. J. Durham, *Phys. Rev. B* **50**, 3861 (1994).
- [46] V. Antonov, B. Harmon, and A. Yaresko, *Electronic Structure and Magneto-Optical Properties of Solids* (Kluwer, Dordrecht, 2004).
- [47] V. N. Antonov, O. Jepsen, A. N. Yaresko, and A. P. Shpak, *J. Appl. Phys.* **100**, 043711 (2006).
- [48] V. N. Antonov, B. N. Harmon, A. N. Yaresko, and A. P. Shpak, *Phys. Rev. B* **75**, 184422 (2007).
- [49] V. N. Antonov, A. N. Yaresko, and O. Jepsen, *Phys. Rev. B* **81**, 075209 (2010).
- [50] V. N. Antonov, L. V. Bekenov, and D. A. Kukusta, *Phys. Rev. B* **102**, 195134 (2020).
- [51] V. V. Nemoshkalenko, A. E. Krasovskii, V. N. Antonov, V. N. Antonov, U. Fleck, H. Wonn, and P. Ziesche, *Phys. Status Solidi B* **120**, 283 (1983).
- [52] J. P. Perdew, K. Burke, and M. Ernzerhof, *Phys. Rev. Lett.* **77**, 3865 (1996).
- [53] P. E. Blöchl, O. Jepsen, and O. K. Andersen, *Phys. Rev. B* **49**, 16223 (1994).
- [54] A. N. Yaresko, V. N. Antonov, and P. Fulde, *Phys. Rev. B* **67**, 155103 (2003).
- [55] P. H. Dederichs, S. Blügel, R. Zeller, and H. Akai, *Phys. Rev. Lett.* **53**, 2512 (1984).
- [56] W. E. Pickett, S. C. Erwin, and E. C. Ethridge, *Phys. Rev. B* **58**, 1201 (1998).
- [57] K. Lie, R. Hoier, and R. Brydson, *Phys. Rev. B* **61**, 1786 (2000).
- [58] S.-D. Mo and W. Y. Ching, *Phys. Rev. B* **62**, 7901 (2000).
- [59] S.-D. Mo and W. Y. Ching, *Appl. Phys. Lett.* **78**, 3809 (2001).
- [60] Y.-N. Xu, Y. Chen, S.-D. Mo, and W. Y. Ching, *Phys. Rev. B* **65**, 235105 (2002).



- [61] W.-Y. Ching, S.-D. Mo, and Y. Chen, *J. Am. Ceram. Soc.* **85**, 11 (2002).
- [62] T. Mizoguchi, I. Tanaka, S. Yoshioka, M. Kunisu, T. Yamamoto, and W. Y. Ching, *Phys. Rev. B* **70**, 045103 (2004).
- [63] H. Ikeno and T. Mizoguchi, *Microscopy* **66**, 305 (2017).
- [64] L. Sandratskii, *Adv. Phys.* **47**, 91 (1998).
- [65] V. N. Antonov, A. P. Shpak, and A. N. Yaresko, *Low Temp. Phys.* **34**, 1 (2008).
- [66] V. N. Antonov, D. A. Kukusta, L. Uba, A. Bonda, and S. Uba, *Phys. Rev. B* **103**, 235127 (2021).